CT Image-Derived Fluctuations in Total Curvature Characterize Aortic Disease Evolution and Clinical Outcomes

Kameel Khabaz[1], Seth Sankary[1], Karen Yuan[1], Joseph Pugar[2], David Jiang[1], Sanjeev Dhara[1], Junsung Kim[1], Janet Kang[1], Nhung Nguyen[1], Kathleen Cao[1], Newell Washburn[2], Nicole Bohr[1], Cheong Jun Lee[3], Gordon Kindlmann[4], Ross Milner[1] and Luka Pocivavsek[1*]

[1]Department of Surgery, The University of Chicago, 5841 S. Maryland Ave., Chicago, 60637, IL, USA.
[2]Departments of Material Science and Engineering, Biomedical Engineering, and Chemistry, Carnegie Mellon University, 5000 Forbes Ave., Pittsburgh, 15213, PA, USA.
[3]Department of Surgery, NorthShore University Health System, 2650 Ridge Ave., Evanston, 60201, IL, USA.
[4]Department of Computer Science, The University of Chicago, 5730 S. Ellis Ave., Chicago, 60637, IL, USA.

*Corresponding author(s). E-mail(s): lpocivavsek@bsd.uchicago.edu;

Abstract

Clinical imaging modalities are a mainstay of modern disease management, but the full utilization of imaging-based treatment algorithms remains elusive. Aortic disease management has been defined by anatomic scalars, even though aortic disease progression initiates complex shape changes which are difficult to quantify. We present an imaging-based geometric descriptor, inspired by fundamental ideas from topology and soft-matter physics, that captures dynamic shape evolution. The fluctuation in total curvature ($\boldsymbol{\delta K}$) captures heterogeneous morphologic evolution by characterizing local shape changes. We discover that aortic morphology evolves with a power-law like behavior with rapidly increasing $\boldsymbol{\delta K}$ forming the hallmark of aortic disease. Classification accuracy for predicting aortic disease state (normal, mildly diseased with successful surgery, and severely diseased with failed surgical

outcomes) approaches $\mathbf{92.8 \pm 1.7\%}$. The analysis of $\boldsymbol{\delta K}$ can be applied on any 3D geometric structure and thus may be extended to other clinical problems of characterizing disease through captured anatomic changes.

Keywords: imaging, shape, aorta, geometry, machine learning

1 Introduction

Imaging modalities such as computed tomography (CT) provide sophisticated three-dimensional representations of the human body and are ubiquitously relied upon to inform clinical practice. At its core, imaging captures anatomic and geometric changes that are linked to underlying pathologic processes. Examples as broad as pulmonary nodules [1], liver cirrhosis [2], and thyroid masses [3, 4] illustrate the deep connection between disease and geometry.

Recent work has sought to translate successes from deep learning (DL) to utilize imaging for disease diagnosis and clinical planning [5, 6]. Challenges in the availability of high-quality data [7, 8], the lack of reproducibility and generalizability [9, 10], the disconnect between technical accuracy and clinical efficacy [11, 12], and interpretability of inherently "black-box" DL models have made the application of DL in medicine particularly fraught [13, 14]. Furthermore, medicine's patient-centered ethos is understandably risk averse, and the trust physicians place in algorithmic models is inversely proportional to the risk of an intervention. DL's challenges magnify physicians' lack of trust in novel approaches for making high-stakes clinical decisions [15, 16].

We take a fundamentally grounded approach in developing imaging-based geometric descriptors of disease evolution in clinically meaningful systems. Aortic dissections, a tear in the wall of the body's largest artery, provide an ideal model system to understand the intersection between measurable geometric change and clinical outcomes. Aortic dissections produce a dynamic and volatile environment leading to complex shape changes [17, 18]. The current standard of care for type B aortic dissection (TBAD) is anchored on the concept of preventing "dangerous" shape changes, such as degeneration into aneurysmal growth, which contribute to worse outcomes [19, 20]. Thus, the concept of shape and pathology are well-accepted; however, our ability to quantify these changes remains limited.

Current medical decision making uses maximum diameter ($2R_m$) to describe geometric change [19], yet clinicians have long appreciated that size is an inadequate descriptor of aortic anatomy [18, 19, 21–23] and have resorted to qualitative descriptors that underpin the complex morphologic evolution accompanying aortic disease. The local geometry of any surface is defined by its principal curvatures, k_1 and k_2. Specific measures of aortic shape have focused on functions of mean ($\kappa_m = (k_1+k_2)/2$) or Gaussian ($\kappa_g = k_1 k_2$) curvature [24, 25], cross-sectional deviations [26], and calculations on centerline reductions of the aortic surface [22, 27, 28]. Despite these efforts, a mathematically robust and reproducible definition of aortic shape does not exist.

Current methods suffer from spatial over-reduction and convolution of shape and size information. Centerline calculations lose information when the aortic surface deforms heterogeneously [29], and κ_g, the dominant shape function, proves itself an ill-defined shape measure because it convolutes shape versus size changes [29].

Here, we develop and validate a size-independent shape measure, the fluctuation in total curvature (δK), that captures heterogeneous morphologic evolution by characterizing local shape changes. We hypothesize and demonstrate that this measure correlates with aortic disease evolution and can be used to characterize treatment response for TBAD.

2 Methods

2.1 Clinical Data Cohort

We analyze a cohort of 302 computed tomography angiography (CTA) scans from 2009 and 2020; 131 scans of diseased aortas and 171 of non-pathologic aortas. Of the 131 scans of diseased aortas, 124 scans are for 36 TBAD patients and 7 scans are for thoracic aortic aneurysm. Three patient subgroups are derived from the main cohort to analyze geometric predictors of outcomes for thoracic endovascular aortic repair (TEVAR) for TBAD: a control cohort, a failed TEVAR cohort, and a successful TEVAR cohort. The control cohort consists of 171 scans of non-pathologic aortas (Table 1). Failed repair is defined as reintervention or type IA endoleak in the follow-up period (using the most recent data available).

A balanced cohort of 18 patients with desired outcomes and 18 patients with failed outcomes is analyzed. Patients all met the inclusion criteria of having both a pre-operative and post-operative CTA. A total of 45 scans (18 pre-operative, 27 post-operative) is included for the desired outcomes group and 51 scans (18 pre-operative, 33 post-operative) is included for the failed outcomes group. Demographic, disease, and imaging information for this group summarized in Table 2.

2.2 Geometric Parameterization

Three-dimensional aortic models are created from CTA image data using a custom workflow in SIMPLEWARE SCANIP (S-2021.06-SP1, Synopsys, Mountain View, CA). Segmentation of the aortic geometry from the scans is processed using a five-step smoothing algorithm to reduce noise, isolate the outer surface, and generate the mesh. A representative schematic of the process is shown in Supplementary Fig. S1 and Supplementary Section 1.2. A triangular mesh for the outer surface is generated for each smoothed segmentation in SCANIP for analysis in MATLAB (2021b, Mathworks, Natick, MA). A total of 15 meshed surfaces are generated for each segmentation (sampling 5 mesh densities and 3 smoothing variations), allowing for control of process-derived variance in surface curvature calculations.

We utilize the Rusinkiewicz algorithm to calculate the per-vertex principal curvatures, k_{1i} and k_{2i}. Briefly, the algorithm calculates the per-vertex shape operator as a weighted average of the shape operators of immediately adjacent faces. The per-face tensors are computed using a finite-difference approximation defined in terms of the

directional derivative of the surface normal [30] (see Supplementary section 1.3 and 1.5 for algorithm details).

2.3 Shape and Size Characterization

Aortic size is parameterized using the centerline length $\mathcal{L}$ and cross-sectional aortic extent ℓ. While $\mathcal{L}$ is singular for each aorta, ℓ is a distribution especially in diseased aortas with heterogeneous shapes. Multiple values can be used to represent this distribution to characterize aortic size: mean aortic radius ($\langle R \rangle$), median aortic radius ($\widetilde{R_2}$), and aortic diameter $2R_m$. ℓ can be calculated directly from surface curvatures as the inverse mean Casorati curvature, $\langle C^{1/2} \rangle^{-1}$, with $C^{1/2}$ defined as the square of the mean Frobenious norm of the per-vertex shape operator $\mathbb{S}_i = \begin{bmatrix} k_{1i} & 0 \\ 0 & k_{2i} \end{bmatrix}$ [31–33]. Higher order functions of size such as total aortic area, A_T, and aortic volume, V, are calculated directly from the meshed surface segmentations.

Fluctuation in total curvature (δK), a generalized size-invariant shape measure, is calculated as variance of total curvature across the surface of a Gauss map of local regions. The Gauss map defines a normalized space where all surface shapes could be compared irrespective of their size [29, 34]. Fig. 1 outlines our computational methodology where we implement the Gauss map by calculating the total curvature (see Supplementary section 1.6 through 1.10 for computational details): $K = \iint_A \kappa_{\mathrm{g}} dA$. To calculate K using extrinsic geometry of highly heterogeneous surfaces, A_T is subdivided into k partitions of area A_j and the calculation is performed at two levels: the partition level and the manifold level (entire aorta). At the partition level, enforcing weak κ_g spatial variation by minimizing the Jensen-Shannon divergence of κ_{gi} allows for the approximation $K_j \approx A_j \bar{\kappa}_{\mathrm{g}j}$. On the manifold level, the sum in total curvature (a topologic invariant) is calculated as ΣK_j, and fluctuation in total curvature is calculated as:

$$\delta K = \frac{1}{A_T} \sum_{j=1}^{k} K_j^2 A_j - \left(\frac{1}{A_T} \sum_{j=1}^{k} K_j A_j \right)^2$$

2.4 Aortic Feature Space Classification using Machine Learning

The classification accuracy of different shape and size metrics in determining aortic disease states (non-pathologic aortas, successful TEVAR, and failed TEVAR) is calculated using the means of the distributions, the mean of the means of the distributions, and a logistic regression classification.

The distribution mean-based methods model is reflective of current clinical practice, in which clinicians are more cognizant of the characteristics of a ”typical” patient in each group (the mean) and are less aware of the variation within each group (the standard deviation). The first model defines each threshold t as the mean value of the parameter for the two neighboring distributions. After these boundaries are defined, each scan is assigned a ”predicted” classification according to its geometric characteristic, and the accuracy of the predictions is computed. The second

model defines each threshold as the mean value of the means of the two neighboring distributions.

A multinomial logistic regression with 1000 random permutations of train-test splits with a 50% training and 50% testing distribution is used for the third model. The variability of the logistic decision boundary includes lasso regularization applied to only $\langle C^{1/2} \rangle$ to examine the impact of increasing the model's dependence on shape over size. Two decision boundaries are created using two binomial logistic regression classifiers, each with regularization applied. The hyperparameter λ is varied to understand the impact of decreasing the influence of size on clinical decision-making to maximize the impact of using a shape-based classifier. The objective function is the penalized negative binomial log-likelihood. See Supplementary Section 5 for more details.

3 Results

The analysis includes a variety of size measures previously described in the literature, including the traditional metric of maximum diameter ($2R_m$) and higher-dimensional values of area or volume (Fig. 2). When each length scalar is plotted versus maximum diameter, the data collapses onto lines, with linear size measures having a slope of 1 and higher-dimensional measures ($\sqrt{A_T}$ and $V^{1/3}$) having slopes that correspond to modeling aortic size as a generalized cylinder ($A_T \sim 2\pi c\ell^2$ and $V \sim \pi c\ell^3$, aortic axial length $\mathcal{L} \sim c\ell$) with a constant independently-calculated prefactor c (see Supplementary Fig. S7). Normalization with the above pre-factors collapses all size measures onto a single common line, consistent with a generalized cylindrical geometry irrespective of surface distortion (Fig. 2).

Application of a (δK, ℓ^{-1})-feature space to a set of eight aortas representative of the normal growth and development of the human aorta and subsequent disease-related degeneration demonstrates two key phases of aortic geometry change. In the first regime, the aorta demonstrates shape-preserving size growth. Aberrant processes such as aortic dissection and aneurysmal degeneration shift the morphogenesis paradigm into the second regime, one characterized by fluctuation in shape as defined by changes in δK (Fig. 3 I). These trends persist across a cohort of 302 segmentations ranging from a healthy 1-year-old child to a highly diseased 92-year-old (see Supplementary Section 1.1).

Fig. 3 examines this generalization phenomenon in the $(\delta K, \ell^{-1})$)-feature space, in which ℓ indicates aortic cross-sectional size and δK, the fluctuation in total curvature, indicates shape divergence. Normalized inverse size $\tilde{\ell}^{-1} = \ell^{-1}/\langle \ell \rangle_{norm}^{-1}$, where $\langle \ell \rangle_{norm}$ is the mean of the normal aortas. All aortas reside on a line above $\sum K = 0$ and cluster with perfect tori and cylinders. By the Gauss-Bonnet theorem, aortic topologic invariance implies that as aortas deform, be it through normal growth or pathology, every increase in K somewhere must be balanced by a proportional decrease elsewhere on the aortic surface [29, 34]. Therefore, the distribution of K across the aortic surface holds information about shape. Since ΣK is constant, the variance $\delta K = \langle K^2 \rangle - \langle K \rangle^2$ captures the balance of positive and negative curvature regions across the surface and is a measure of shape deformation. When

$\widetilde{\delta K} = \delta K/\min|\delta K|$ is plotted against $\tilde{\ell}^{-1}$, the geometric signature of shape preserving growth seen in normal aortas (black circles) is a small and nearly constant $\widetilde{\delta K}$ (Fig. 3 II). Following the yellow symbols, corresponding to the representative segmentations in Fig. 3 I, allows a direct visual comparison between the development of pathology and the divergence of $\widetilde{\delta K}$. In the $(\widetilde{\delta K}, \tilde{\ell}^{-1})$-space the data fits to a power law $\widetilde{\delta K} = 2(1/\tilde{\ell})^{-4} + 1$ (Fig. 3 III). The existence of a power law behavior is further supported by the power-law probability distribution of δK (Supplementary Fig. S8).

The strong correlation between δK divergence and the evolution of aortic pathology begs application to treatment planning. Fig. 4 compares the effectiveness of aortic size, the clinical standard, with the $(\delta K, \ell^{-1})$ shape-size feature space in determining aortic disease states (non-pathologic aortas, successful TEVAR, and failed TEVAR). Significant variability in aortic size within the broader patient population is captured even by this limited single institutional dataset. Furthermore, there is overlap between the normal and diseased populations and as such, classification accuracy dramatically changes due to slight differences in model parameterizations (from 73% in Fig. 4 Ia, 83.9% in Fig. 4 Ib, and $86.6 \pm 2.2\%$ in Fig. 4 Ic). The dual parameterization of both aortic size and shape — two orthogonal metrics — expands the geometric characterization into a two-dimensional space (Fig. 4 II). Classification accuracy increases to 90.3% in Fig. 4 IIa and $92.8 \pm 1.7\%$ in Fig. 4 IIb. A subset analysis using the $(\delta K, \ell^{-1})$-space of five patients with long-term follow-up and failed post-surgical outcomes identifies diseased aortas in approximately the same size range but with significantly different shape deformity (δK) compared to successful TEVAR (see Supplementary Fig. S12).

As shown in Fig. 5-Ia, there is no significant difference amongst size predictors from the literature, including those shown in Fig. 2 as well as Gaussian-curvature based measures like the L2-norm of the Gaussian curvature (GLN) and the area-averaged Gaussian curvature (GAA). The major difference is with shape measures: clinical shape measures, which are based on the aortic centerline, significantly underperform δK in aortic disease state classification (Fig. 5-Ib). Similarly, δK outperforms other shape measures described in the biomedical engineering literature (Fig. 5-Ic; see Supplementary Section 5 for more information).

4 Discussion

Type B aortic dissection (TBAD) is a life-threatening disease with significant associated morbidity and mortality. [17–19]. While the old paradigm of open surgical repair was fraught with peri-operative risk, new minimally invasive approaches (thoracic endovascular aortic repair, or TEVAR) have raised the specter of long-term risk including device failure. Proper identification of patients for endovascular repair is therefore critical and necessitates the definition of an appropriate classification scheme [19, 21, 23, 35]. While previous work has focused on linking changes in aortic anatomy and suitabiltity for repair, there remains a dire need to improve our understanding of how best to define geometric changes and to understand their impact on patient outcomes.

Projection of aortic anatomy into the $(\delta K, \ell^{-1})$-space provides an improved ability to differentiate aortas along the entire spectrum of growth and pathology, including both normal size-related development and pathologic shape-related changes. We demonstrate that in normal conditions, the aorta undergoes shape-invariant growth (see Fig. 3 I), while, in diseased states, the aorta experiences shape fluctuations defined by increasing δK. As shown in Fig. 5, δK significantly outperforms all other available measures of shape in predicting clinical treatment outcomes, including tortuosity, which is prevalent in the clinical arena.

Furthermore, because of the invariant global cylindrical geometry of the aorta, the parameterization of size is dependent only on the single length scale ℓ^{-1}. Higher-dimensional characterizations of size, including area A_T and volume V, do not provide additional information [36, 37]. Thus, current efforts to replace $2R_m$ with area or volume [36, 37] are unlikely to yield substantially more information (Fig. 5). This universal size scaling provides the quantitative basis behind the utility of maximum diameter throughout the decades of aortic management and further validates the study of shape [23].

Fig. 4 compares the efficacy of a single-variable space defined by maximum diameter ($2R_m$), the clinical standard, with an enhanced shape-size feature space for predicting treatment outcomes. Using size as the sole metric of disease change, the cornerstone of imaging-based practice in other clinical contexts, is inherently problematic because a critical point between closely-spaced and overlapping populations is very sensitive to the available data. For instance, a well-known problem in R_m-based criteria is the bias against smaller statured female patients because of the heavily male-weighted population-based statistics [38, 39]. This is best illustrated by Fig. 4. While arbitrarily defined size classifiers did discriminate amongst normal aortas, successful TEVAR, and failed TEVAR, such scalars lack physical meaning and clinical generalizability outside of the specific cohort being analyzed. This is partly due to natural population-level variation in aortic size in addition to the inherently operator-dependent nature of aortic size measurements (such as diameter) [40].

The addition of the second axis (δK) alleviates this issue by providing a quantifiable and reproducible shape scalar. δK also captures the global geometry of the aorta and is operator independent. The combined (δK, ℓ^{-1})-feature space demonstrates greater than 90% classification accuracy for the same three cohorts. The addition of a tangible shape axis also offers enhanced interpretability of the underlying geometric trends driving aortic pathology. Such a classification space can be clinically applied to pre-operative treatment planning for aortic dissection patients (see Supplementary Section 5). δK outperforms previously described shape metrics in both the clinical and engineering literatures. Clinically-derived shape measures, such as tortuosity index, are predominately acquired from aortic centerlines [22, 41]. These measures underperform compared to δK and are no better than ℓ^{-1} alone for characterizing aortic disease pathology from geometry (see Supplementary Table S1). As such, future analysis of δK is liable to demonstrate substantial clinical application of δK as a clinical outcomes predictor.

No general theory exists on the meaning of δK divergence. In soft matter systems such as spherical vesicles, where size weakly changes, and in dynamic systems, rapid

fluctuations of Gaussian curvature have been linked to so-called 'topologic catastrophes' indicative of physical instability [32, 33, 42]. While we do not inherently study aortic stability as it relates to clinical rupture, we show that aortas with high δK independently classify as high risk for clinical complications and poor outcomes. It is therefore reasonable to conjecture that vertical divergence in the $(\widetilde{\delta K}, \tilde{\ell}^{-1})$-space is a sign of aortic instability and an indicator of suboptimal suitability for endovascular repair.

The morphologic evolution of biological structures is tightly integrated with disease development in many other contexts. δK is a size-independent shape metric, and because it only requires extrinsic geometric information, this procedure can be applied to any surface mesh geometry. For instance, 3D imaging is extensively used to analyze lung nodules for malignancy [1], breast lesions for tumor growth [43], liver irregularities for cirrhosis [2], cerebral aneurysms [44], and the left ventricle for heart failure [45].

As with the aorta, size-based criteria form the mainstay of clinical approaches, while shape is qualitatively used but has been proven difficult to quantify until now. This methodology is based on a general geometric and topologic foundation, and future analysis will be needed to validate its extension to other clinically-relevant problems of characterizing disease through analysis of shape change in medical imaging.

Acknowledgments: We acknowledge the support of the National Institutes of Health, NHLBI, R01HL159205. We are grateful to Enrique Cerda, Efi Efrati, Haim Diamant, and Thomas Witten for careful reading of the text and detailed comments.

Demographics (N = 93)	N	%		
Male	66	71		
Female	27	29		
White	9	5.6		
Declined	2	5.6		
Black	75	83		
Other	7	5.6		
	Mean	SD	Min	Max
Age	37.08	18.10	1	86
Comorbidities	N	%		
Diabetes	6	6.4		
Hypertension	11	11.8		
COPD	5	5.4		
Smoking	9	9.7		
Coronary Artery Disease (CAD)	2	2.2		
Peripheral Artery Disease (PAD)	0	0		
Heart Failure	3	3.2		
Stroke	0	0		

Table 1 Non-Pathologic Aortic Cohort Patient Information

Demographics (N = 36)	N	%		
Male	21	58		
Female	15	42		
White	9	25		
Declined	2	5.6		
Black	22	61		
Other	3	8.3		
	Mean	SD	Min	Max
Age	63.25	13.88	36	93
Comorbidities	N	%		
Hypertension	32	94		
Known Marfan	0	0		
Chronic Obstructive Pulmonary Disease (COPD)	7	21		
Smoking	24	71		
Coronary Artery Disease (CAD)	11	32		
Peripheral Arterial Disease (PAD)	4	12		
Heart Failure	9	26		
Diabetes	4	12		
Stroke	4	12		
Acute TBAD	3	8.8		
Complicated TBAD	3	8.3		
Device Information	Mean	SD	min	max
# Devices	2.08	1.20	1	6
# Reinterventions	1.33			
Proximal Oversizing	20%	0.104%	2%	48%
	N	%		
Z3 Landing Zone	21	58		
Z2 Landing Zone	12	33		
Z1 Landing Zone	2	6		
Z0 Landing Zone	1	3		
Medtronic® Navion Device	25	69		
Gore® TAG® Device	10	28		
Cook® TX2® Device	1	3		
Reintervention	15	42		
Endoleak	16	50		
Imaging Data	Mean	SD	min	max
Follow Up Time (Years)	1.78	1.69	0.074	5.85
# Total CTA Scans	6.81	2.91	3	15
Time to Intervention	1.33	2.36	0	9.61
# Post-op CTA Scans	4	2.26	1	11

Table 2 Type B Aortic Dissection Cohort Patient Information

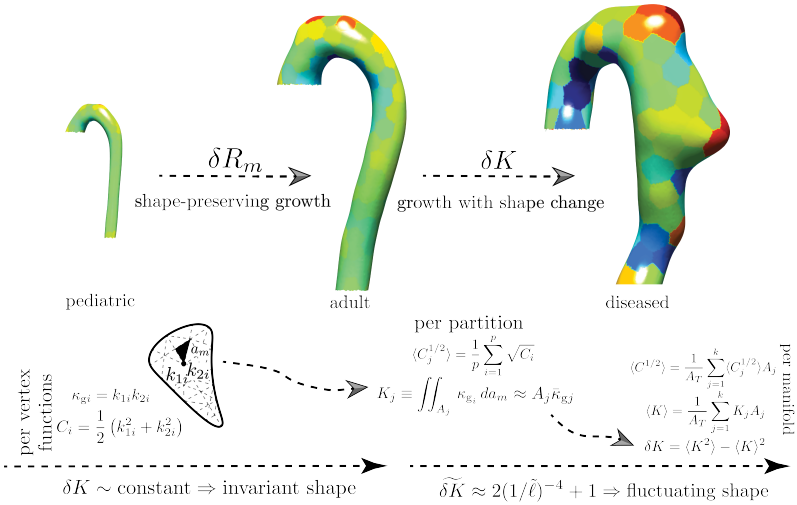

Fig. 1 By mapping the aortic surface to the unit sphere (Gauss map [29]), we have an independent measure of shape. The per-vertex shape operator $\mathbb{S}_i$ is calculated using the Rusinkiewicz algorithm [30]. To minimize noise, the aorta is partitioned into multiple patches with area A_j. The local integrated Gaussian curvature K_j is calculated as the product of patch area and mean Gaussian curvature, $\bar{\kappa}_{\mathrm{g}j}$ (see Supplementary Methods). K_j is equivalent to the signed patch area $\widetilde{A_j}$ mapped out by the normals projected onto the unit sphere. We define aortic shape by studying the statistics of the distributions of K_j. $\langle K \rangle$ and δK are the first and second distribution moments that define aortic shape geometry, respectively. Fig. 3-III shows that δK is a powerful variable with which to track aortic shape changes.

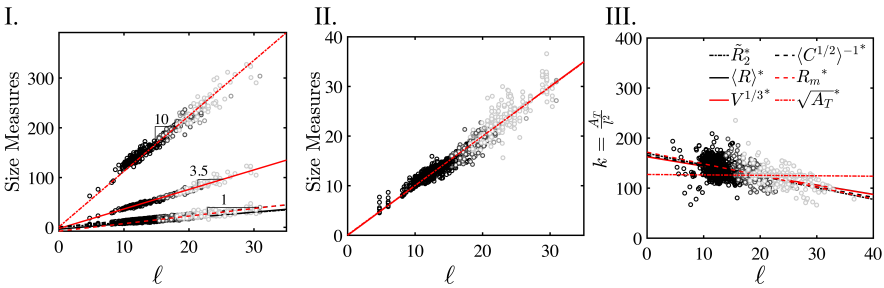

Fig. 2 Data for 302 aortas, including non-pathologic (black circles), pathologic with failed TEVAR (light gray circles), and pathologic with successful TEVAR (dark gray circles) aortas are plotted. **I.** shows that parameterizations of aortic size (mm) including mean radius ($\langle R \rangle$, black solid line), median radius ($\widetilde{R_2}$, black dotted line), and mean inverse linearized aortic Casorati curvature ($\langle C^{1/2} \rangle^{-1}$, black dashed line) are equivalent. Dimensionally scaled, aortic area ($\sqrt{A_T}$, red dotted line) and volume ($V^{1/3}$, red solid line) are also linear when plotted against $\ell = 2R_m$. All size measures can be collapsed onto a single master curve (**II.**), proving that all aortas scale as generalized bent cylinders parameterizable by a single length scale ℓ. **III.** The linear scaling can be used to define $A_j \sim \ell^2$, which sets the number of partitions k used in the Gauss map calculations.

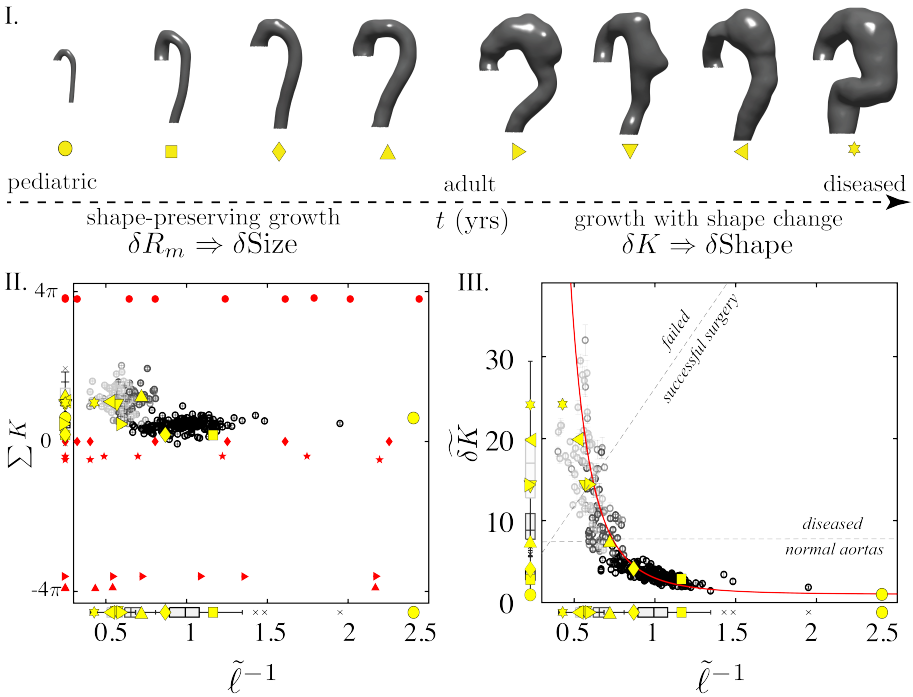

Fig. 3 **I.** Eight representative aortas along the normal-to-diseased axis (left to right): a 1-year-old child, healthy adults, and type B aortic dissection (TBAD) patients at varying degrees of aneurysmal degeneration. Two clinical regimes exist: shape preserving growth and growth with shape changes. **II.** shows the topologic equivalence of all aortic shapes to tori (red stars) and cylinders (red diamonds); the yellow symbols correspond to specific aortic shapes along the normal-to-diseased axis (**I.**). Red circles correspond to perfect spheres of varying size; pseudospheres and catenoids are depicted as red rightward-pointing triangles and upward-pointing triangles, respectively. **III.** shows the optimal two-dimensional aortic geometric feature space with independent axes for size and shape. The solid red line, $\widetilde{\delta K} = 2(1/\tilde{\ell})^{-4} + 1$, is a best fit to the data. The power-like behavior is further supported by the probability distribution of δK (Supplementary Fig. S8). The aortas separate into shape invariant (normal) and shape fluctuating (diseased) populations. Furthermore, this feature space defines decision boundaries which correctly classify diseased patients based upon success of TEVAR (Fig. 4).

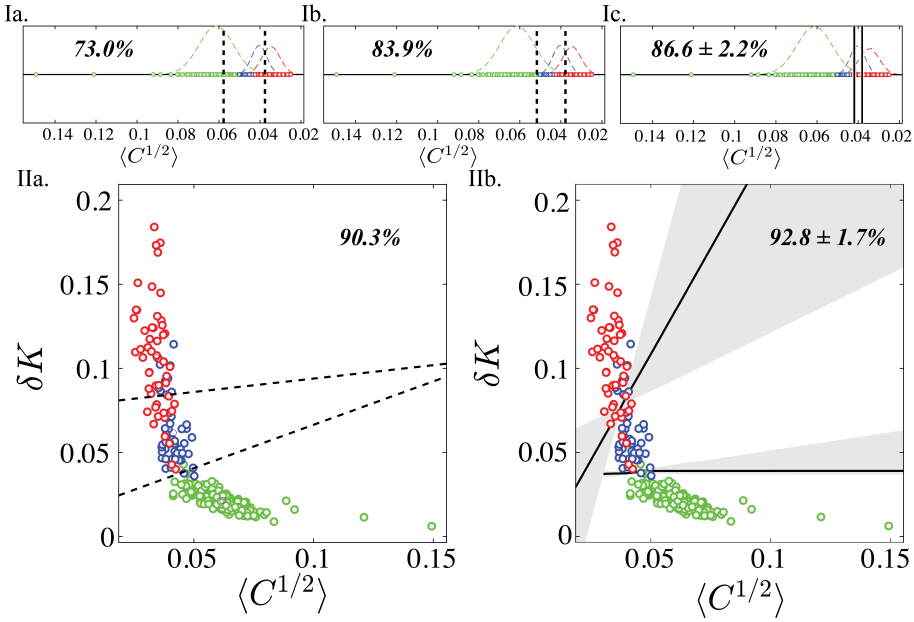

Fig. 4 The $(\delta K, \ell)$ geometric feature space improves upon current sized-based methods. I. The clinical paradigm relies on size metrics alone to classify aortic disease states (green for non-pathologic aortas, blue for successful TEVAR, and red for failed TEVAR). However, broad within-group size distributions indicate the considerable variability in aortic sizes within the general population. Clinicians routinely utilize statistical means of these distributions as thresholds for classifying disease states, but linear decision boundaries are highly sensitive to small changes in model setup. Ia. A 73.0% accuracy for classifying the 3 disease states is obtained when each threshold is defined as the mean $\langle C^{1/2} \rangle$ of the two neighboring distributions. Ib. An 83.9% accuracy is achieved when the threshold is defined as the midpoint of the means of individual class distributions. Ic. A 86.6% mean accuracy is obtained when a logistic regression classifier is used. Thus, small changes in how a threshold is defined dramatically alter the perceived utility of size. II. The $(\delta K, \ell)$ shape and size-based geometric feature space allows for the utilization of two independent parameters to characterize aortic disease state. IIa. A 90.3% classification accuracy is obtained when defining thresholds according to the mean δK and $\langle C^{1/2} \rangle$ of each patient group. IIb. A 92.8% mean accuracy with a standard deviation of only 1.7% is obtained using a logistic regression classifier with varying regularization parameter. The shaded region indicates the interquartile range of decision boundaries and demonstrates the robustness of the two-parameter space. Unlike the single parameter space, the presence of two physically interpretable and orthogonal asymptotic limits ensures more effective classification.

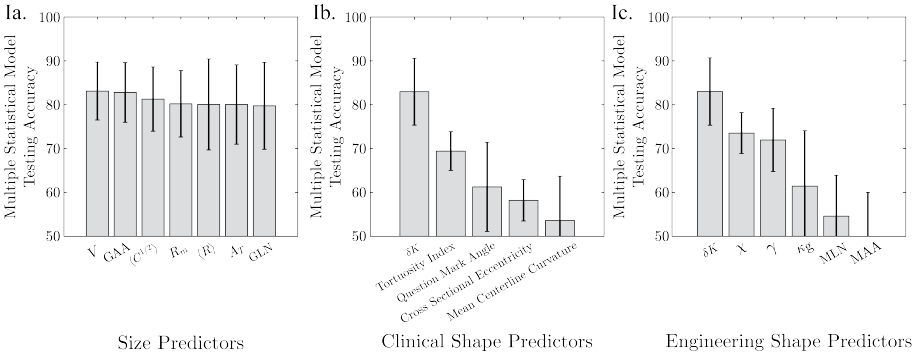

Fig. 5 Comparison of size and shape metrics in classifying aortic disease state from medical imaging. Ia. Measures of aortic size achieve similar classification accuracies and thus are functionally equivalent (corroborating Fig. 2). The GLN and GAA are other size metrics, as shown in Supplemenatry Fig. S11. Ib. δK significantly outperforms measures of aortic shape from the clinical literature in classifying aortic disease state (normal non-diseased aortas, diseased aortas with desired outcomes following TEVAR, and aortas with failed outcomes following TEVAR). Ic. δK outperforms general shape metrics from the broad engineering literature (shown in Supplemenatry Fig. S11). Error bars indicate ± 1 standard deviation of the classification accuracies for the different classification methods.

References

[1] Annemie Snoeckx, Pieter Reyntiens, Damien Desbuquoit, Maarten J. Spinhoven, Paul E. Van Schil, Jan P. van Meerbeeck, and Paul M. Parizel. Evaluation of the solitary pulmonary nodule: size matters, but do not ignore the power of morphology. *Insights into Imaging*, 9(1):73–86, February 2018. Number: 1 Publisher: SpringerOpen.

[2] P P Anthony, K G Ishak, N C Nayak, H E Poulsen, P J Scheuer, and L H Sobin. The morphology of cirrhosis. Recommendations on definition, nomenclature, and classification by a working group sponsored by the World Health Organization. *Journal of Clinical Pathology*, 31(5):395–414, May 1978.

[3] Eisuke Koike, Shiro Noguchi, Hiroyuki Yamashita, Tsukasa Murakami, Akira Ohshima, Hitoshi Kawamoto, and Hiroto Yamashita. Ultrasonographic Characteristics of Thyroid Nodules: Prediction of Malignancy. *Archives of Surgery*, 136(3):334–337, March 2001.

[4] Zubair W. Baloch, Virginia A. LiVolsi, Syl L. Asa, Juan Rosai, Maria J. Merino, Gregory Randolph, Philippe Vielh, Richard M. DeMay, Mary K. Sidawy, and William J. Frable. Diagnostic terminology and morphologic criteria for cytologic diagnosis of thyroid lesions: A synopsis of the National Cancer Institute Thyroid Fine-Needle Aspiration State of the Science Conference. *Diagnostic Cytopathology*, 36(6):425–437, 2008. _eprint: https://onlinelibrary.wiley.com/doi/pdf/10.1002/dc.20830.

[5] Andre Esteva, Alexandre Robicquet, Bharath Ramsundar, Volodymyr Kuleshov, Mark DePristo, Katherine Chou, Claire Cui, Greg Corrado, Sebastian Thrun, and Jeff Dean. A guide to deep learning in healthcare. *Nature Medicine*, 25(1):24–29, January 2019. Number: 1 Publisher: Nature Publishing Group.

[6] Satya P. Singh, Lipo Wang, Sukrit Gupta, Haveesh Goli, Parasuraman Padmanabhan, and Balázs Gulyás. 3D Deep Learning on Medical Images: A Review. *Sensors*, 20(18):5097, September 2020.

[7] Hussein Ibrahim, Xiaoxuan Liu, Nevine Zariffa, Andrew D. Morris, and Alastair K. Denniston. Health data poverty: an assailable barrier to equitable digital health care. *The Lancet Digital Health*, 3(4):e260–e265, April 2021. Publisher: Elsevier.

[8] Daniel A. Hashimoto, Guy Rosman, Daniela Rus, and Ozanan R. Meireles. Artificial Intelligence in Surgery: Promises and Perils. *Annals of surgery*, 268(1):70–76, July 2018.

[9] Félix Renard, Soulaimane Guedria, Noel De Palma, and Nicolas Vuillerme. Variability and reproducibility in deep learning for medical image segmentation. *Scientific Reports*, 10(1):13724, August 2020.

[10] Matthew B. A. McDermott, Shirly Wang, Nikki Marinsek, Rajesh Ranganath, Luca Foschini, and Marzyeh Ghassemi. Reproducibility in machine learning for health research: Still a ways to go. *Science Translational Medicine*, 13(586):eabb1655, March 2021. Publisher: American Association for the Advancement of Science.

[11] Pearse A. Keane and Eric J. Topol. With an eye to AI and autonomous diagnosis. *npj Digital Medicine*, 1(1):1–3, August 2018. Number: 1 Publisher: Nature Publishing Group.

[12] Christopher J. Kelly, Alan Karthikesalingam, Mustafa Suleyman, Greg Corrado, and Dominic King. Key challenges for delivering clinical impact with artificial intelligence. *BMC Medicine*, 17(1):195, October 2019.

[13] Sandeep Reddy. Explainability and artificial intelligence in medicine. *The Lancet Digital Health*, 4(4):e214–e215, April 2022. Publisher: Elsevier.

[14] Shinjini Kundu. AI in medicine must be explainable. *Nature Medicine*, 27(8):1328–1328, August 2021. Number: 8 Publisher: Nature Publishing Group.

[15] Matthew DeCamp and Jon C. Tilburt. Why we cannot trust artificial intelligence in medicine. *The Lancet Digital Health*, 1(8):e390, December 2019. Publisher: Elsevier.

[16] Onur Asan, Alparslan Emrah Bayrak, and Avishek Choudhury. Artificial Intelligence and Human Trust in Healthcare: Focus on Clinicians. *Journal of Medical Internet Research*, 22(6):e15154, June 2020. Company: Journal of Medical Internet Research Distributor: Journal of Medical Internet Research Institution: Journal of Medical Internet Research Label: Journal of Medical Internet Research Publisher: JMIR Publications Inc., Toronto, Canada.

[17] M. E. De Bakey and D. A. Cooley. Successful resection of aneurysm of thoracic aorta and replacement by graft. *Journal of the American Medical Association*, 152(8):673–676, June 1953.

[18] M. E. De Bakey, D. A. Cooley, and O. Creech. Surgical considerations of dissecting aneurysm of the aorta. *Annals of Surgery*, 142(4):586–610; discussion, 611–612, October 1955.

[19] Thomas E. MacGillivray, Thomas G. Gleason, Himanshu J. Patel, Gabriel S. Aldea, Joseph E. Bavaria, Thomas M. Beaver, Edward P. Chen, Martin Czerny, Anthony L. Estrera, Scott Firestone, Michael P. Fischbein, G. Chad Hughes, Dawn S. Hui, Kalie Kissoon, Jennifer S. Lawton, Davide Pacini, T. Brett Reece, Eric E. Roselli, and John Stulak. The Society of Thoracic Surgeons/American Association for Thoracic Surgery Clinical Practice Guidelines on the Management of Type B Aortic Dissection. *The Annals of Thoracic Surgery*,

113(4):1073–1092, April 2022.

[20] Joseph V. Lombardi, G. Chad Hughes, Jehangir J. Appoo, Joseph E. Bavaria, Adam W. Beck, Richard P. Cambria, Kristofer Charlton-Ouw, Mohammad H. Eslami, Karen M. Kim, Bradley G. Leshnower, Thomas Maldonado, T. Brett Reece, and Grace J. Wang. Society for Vascular Surgery (SVS) and Society of Thoracic Surgeons (STS) reporting standards for type B aortic dissections. *Journal of Vascular Surgery*, 71(3):723–747, March 2020.

[21] Dominik Fleischmann, Rana O. Afifi, Ana I. Casanegra, John A. Elefteriades, Thomas G. Gleason, Kate Hanneman, Eric E. Roselli, Martin J. Willemink, Michael P. Fischbein, and American Heart Association Council on Cardiovascular Radiology and Intervention; Council on Arteriosclerosis, Thrombosis and Vascular Biology; Council on Clinical Cardiology; and Council on Cardiovascular Surgery and Anesthesia. Imaging and Surveillance of Chronic Aortic Dissection: A Scientific Statement From the American Heart Association. *Circulation. Cardiovascular Imaging*, 15(3):e000075, March 2022.

[22] Chun-Ku Chen, I.-Ping Liang, Hsiao-Ting Chang, Wei-Yuan Chen, I.-Ming Chen, Mei-Han Wu, Ming-Huei Sheu, and Chun-Che Shih. Impact on outcomes by measuring tortuosity with reporting standards for thoracic endovascular aortic repair. *Journal of Vascular Surgery*, 60(4):937–944, October 2014.

[23] Domenico Spinelli, Filippo Benedetto, Rocco Donato, Gabriele Piffaretti, Massimiliano M. Marrocco-Trischitta, Himanshu J. Patel, Kim A. Eagle, and Santi Trimarchi. Current evidence in predictors of aortic growth and events in acute type B aortic dissection. *Journal of Vascular Surgery*, 68(6):1925–1935.e8, December 2018.

[24] Judy Shum, Amber Xu, Itthi Chatnuntawech, and Ender A. Finol. A framework for the automatic generation of surface topologies for abdominal aortic aneurysm models. *Annals of Biomedical Engineering*, 39(1):249–259, January 2011.

[25] Kibaek Lee, Junjun Zhu, Judy Shum, Yongjie Zhang, Satish C. Muluk, Ankur Chandra, Mark K. Eskandari, and Ender A. Finol. Surface curvature as a classifier of abdominal aortic aneurysms: a comparative analysis. *Annals of Biomedical Engineering*, 41(3):562–576, March 2013.

[26] Johan Bondesson, Ga-Young Suh, Neil Marks, Michael D. Dake, Jason T. Lee, and Christopher P. Cheng. Influence of thoracic endovascular aortic repair on true lumen helical morphology for Stanford type B dissections. *Journal of Vascular Surgery*, 74(5):1499–1507.e1, November 2021.

[27] G. Giannoglou, G. Giannakoulas, J. Soulis, Y. Chatzizisis, T. Perdikides, N. Melas, G. Parcharidis, and G. Louridas. Predicting the risk of rupture of abdominal aortic aneurysms by utilizing various geometrical parameters:

revisiting the diameter criterion. *Angiology*, 57(4):487–494, 2006.

[28] Da Li, Liqing Peng, Yi Wang, Jichun Zhao, Ding Yuan, and Tinghui Zheng. Predictor of false lumen thrombosis after thoracic endovascular aortic repair for type B dissection. *The Journal of Thoracic and Cardiovascular Surgery*, 160(2):360–367, August 2020.

[29] Tristan Needham. *Visual Differential Geometry and Forms*. Princeton University Press, July 2021.

[30] S. Rusinkiewicz. Estimating curvatures and their derivatives on triangle meshes. In *Proceedings. 2nd International Symposium on 3D Data Processing, Visualization and Transmission, 2004. 3DPVT 2004.*, pages 486–493, September 2004.

[31] Jan Koenderink, Andrea van Doorn, and Johan Wagemans. Local Solid Shape. *i-Perception*, 6(5):2041669515604063, October 2015. Publisher: SAGE Publications.

[32] Oscar F. Aguilar Gutierrez and Alejandro D. Rey. Extracting shape from curvature evolution in moving surfaces. *Soft Matter*, 14(8):1465–1473, February 2018. Publisher: The Royal Society of Chemistry.

[33] James E. McClure, Steffen Berg, and Ryan T. Armstrong. Geometric evolution as a source of discontinuous behavior in soft condensed matter, June 2019. arXiv:1906.04073 [cond-mat, physics:physics].

[34] Jan J. Koenderink. *Solid Shape*. The MIT Press, 1990.

[35] Liang Liang, Minliang Liu, Caitlin Martin, John A. Elefteriades, and Wei Sun. A machine learning approach to investigate the relationship between shape features and numerically predicted risk of ascending aortic aneurysm. *Biomechanics and Modeling in Mechanobiology*, 16(5):1519–1533, October 2017.

[36] Jong-Min Song, Sung-Doo Kim, Jeong-Hoon Kim, Mi-Jeong Kim, Duk-Hyun Kang, Joon Beom Seo, Tae-Hwan Lim, Jae Won Lee, Meong-Gun Song, and Jae-Kwan Song. Long-term predictors of descending aorta aneurysmal change in patients with aortic dissection. *Journal of the American College of Cardiology*, 50(8):799–804, August 2007.

[37] Tae-Hoon Kim, Young-Guk Ko, Sung Woo Kwon, Donghoon Choi, Do Yun Lee, Won-Heum Shim, and Min Su Hyon. Large false lumen area is a predictor of failed false lumen volume reduction after stent-graft repair in type B aortic dissection. *Journal of Endovascular Therapy: An Official Journal of the International Society of Endovascular Specialists*, 21(5):697–706, October 2014.

[38] Ruby C. Lo, Rodney P. Bensley, Allen D. Hamdan, Mark Wyers, Julie E. Adams, Marc L. Schermerhorn, and Vascular Study Group of New England. Gender differences in abdominal aortic aneurysm presentation, repair, and mortality in the Vascular Study Group of New England. *Journal of Vascular Surgery*, 57(5):1261–1268, 1268.e1–5, May 2013.

[39] Manish Mehta, W. John Byrne, Handel Robinson, Sean P. Roddy, Philip S. K. Paty, Paul B. Kreienberg, Paul Feustel, and R. Clement Darling. Women derive less benefit from elective endovascular aneurysm repair than men. *Journal of Vascular Surgery*, 55(4):906–913, April 2012.

[40] Vijayapraveena Paruchuri, Kahled F. Salhab, Gregory Kuzmik, George Gubernikoff, Hai Fang, John A. Rizzo, Bulat A. Ziganshin, and John A. Elefteriades. Aortic Size Distribution in the General Population: Explaining the Size Paradox in Aortic Dissection. *Cardiology*, 131(4):265–272, 2015. Publisher: Karger Publishers.

[41] Viony M. Belvroy, Rodrigo M. Romarowski, Theodorus M. J. van Bakel, Joost A. van Herwaarden, Jean Bismuth, Ferdinando Auricchio, Frans L. Moll, and Santi Trimarchi. Impact of Aortic Tortuosity on Displacement Forces in Descending Thoracic Aortic Aneurysms. *European Journal of Vascular and Endovascular Surgery*, 59(4):557–564, April 2020. Publisher: Elsevier.

[42] Marco Pettini. *Geometry and Topology in Hamiltonian Dynamics and Statistical Mechanics*, volume 33 of *Interdisciplinary Applied Mathematics*. Springer, New York, NY, 2007.

[43] Tingting Mu, Asoke K. Nandi, and Rangaraj M. Rangayyan. Classification of Breast Masses Using Selected Shape, Edge-sharpness, and Texture Features with Linear and Kernel-based Classifiers. *Journal of Digital Imaging*, 21(2):153–169, June 2008.

[44] Clémence Maupu, Héloïse Lebas, and Yacine Boulaftali. Imaging Modalities for Intracranial Aneurysm: More Than Meets the Eye. *Frontiers in Cardiovascular Medicine*, 9:793072, February 2022.

[45] Wolfgang Lieb, Philimon Gona, Martin G. Larson, Jayashri Aragam, Michael R. Zile, Susan Cheng, Emelia J. Benjamin, and Ramachandran S. Vasan. The Natural History of Left Ventricular Geometry in the Community: Clinical Correlates and Prognostic Significance of Change in LV Geometric Pattern. *JACC: Cardiovascular Imaging*, 7(9):870–878, September 2014.